The Astrophysical Journal, 836:28 (7pp), 2017 February 10 https://doi.org/10.3847/1538-4357/836/1/28

Infrared Spectra of Hexa-peri-hexabenzocoronene Cations: HBC^{+} and HBC^{2+}

Junfeng Zhen[1,2], Pablo Castellanos[1,2], Jordy Bouwman[2,3], Harold Linnartz[2], and Alexander G. G. M. Tielens[1]
[1] Leiden Observatory, Leiden University, P.O. Box 9513, 2300 RA Leiden, The Netherlands; zhen@strw.leidenuniv.nl
[2] Sackler Laboratory for Astrophysics, Leiden Observatory, Leiden University, P.O. Box 9513, 2300 RA Leiden, The Netherlands
[3] IMM, FELIX Lab, Radboud University Nijmegen, Toernooiveld 7c, 6525 ED Nijmegen, The Netherlands

Received 2016 December 23; revised 2017 January 13; accepted 2017 January 13; published 2017 February 7

Abstract

We present the first infrared (IR) gas-phase spectrum of a large and astronomically relevant polycyclic aromatic hydrocarbon (PAH) cation ($C_{42}H_{18}^{+}$, HBC^{+}) and its dication ($C_{42}H_{18}^{2+}$, HBC^{2+}). The spectra are recorded via infrared multiphoton dissociation (IRMPD) spectroscopy of ions stored in a quadrupole ion trap, using the intense IR radiation of a free electron laser in the 530–1800 cm^{-1} (5.6–18.9 μm) range. HBC^{+} shows main intense absorption peaks at 762 (13.12), 1060 (9.43), 1192 (8.39), 1280 (7.81), 1379 (7.25), and 1530 (6.54) cm^{-1} (μm), in good agreement with density functional theory calculations after scaling to take the anharmonicities effect into account. HBC^{2+} has its main absorption peaks at 660 (15.15), 766 (13.05), 1054 (9.49), 1176 (8.50), 1290 (7.75), 1370 (7.30) and 1530 (6.54) cm^{-1} (μm). Given the similarity in the cationic and dicationic spectra, we have not identified an obvious diagnostic signature to the presence of multiply charged PAHs in space. While experimental issues associated with the IRMPD technique preclude a detailed comparison with interstellar spectra, we do note that the strong bands of HBC^{+} and HBC^{2+} at ~6.5, 7.7, 8.4, and 13.1 μm coincide with prominent aromatic infrared bands (AIBs). HBC has only trio CH groups, and the out-of-plane CH bending mode of both HBC cations is measured at 13.1 μm, squarely in the range predicted by theory and as previously found in studies of small (substituted) PAHs. This study therefore supports the use of AIBs observed in the 11–14 μm range as a diagnostic tool for the edge topology of large PAHs in space.

Key words: astrochemistry – ISM: abundances – ISM: molecules – molecular data – molecular processes

1. Introduction

The aromatic infrared bands (AIBs) dominate the near- and mid-infrared spectra of many interstellar sources. These bands are generally attributed to infrared (IR) fluorescence of large (~50 C-atoms) polycyclic aromatic hydrocarbon (PAH) molecules after excitation by ultraviolet photons (Sellgren 1984; Allamandola et al. 1989; Puget & Leger 1989; Genzel et al. 1998; Tielens 2013). PAHs are expected to form in the ejecta of AGN stars and are ubiquitous and abundant, containing ~10% of the elemental carbon in the interstellar medium (ISM). They play an important role in the ionization and energy balance of the ISM (Tielens 2008, and references therein). The assignment of the AIBs to PAH molecules has been discussed in several studies (Allamandola et al. 1989; Peeters et al. 2002; Tielens 2005, 2008). Generally, the prominent 3.3 μm band is linked to aromatic CH stretches, the 6.2 and 7.7 μm features are considered to be due to CC vibrations of aromatic rings, and the 8.6 μm as well as the longer wavelength region bands are assigned to CH in- and out-of-plane bending and/or CCC bending vibrations (Tielens 2013).

Infrared spectroscopy provides a powerful tool to study the molecular characteristics of the emitting species. Specifically, for the CH out-of-plane (oop) bending vibrations in the 11–14 μm region, a different number of adjacent CH bonds gives rise to vibrations in distinctly different wavelength regions (Hony et al. 2001; Tielens 2008). These spectroscopic rules on H-adjacency and the positions of the oop modes have largely been derived from experimental studies on small (substituted) aromatic systems such as benzene and naphthalene (Bellamy 1958) and are supported by density functional theory (DFT) calculations (cf. Bauschlicher et al. 2010). Furthermore, laboratory and quantum chemical studies have revealed that the CC stretching modes in the 6–9 μm region are much stronger in ionized PAHs than in their neutral counterparts (Allamandola et al. 1999; Peeters et al. 2002). These three bands (6.2, 7.7, and 8.6 μm), which correlate well, therefore may be attributed to PAH cations. Recent studies, using PAH ions trapped in hydrogen matrices (Tsuge et al. 2016) or measured in tagged ion dissociation studies (Knorke et al. 2009; Ricks et al. 2009), also show nice agreement with vibrational modes recorded for protonated PAH species. This is supported by observational studies that reveal that these bands grow in strength—relative to the CH bands characteristic for neutral PAHs—in regions characterized by high ionization parameters[4]; e.g., close to the illuminating source (Rapacioli et al. 2005; Berné et al. 2007; Boersma et al. 2013). However, in such regions, PAH cations can also be further ionized, resulting in doubly, triply, or even higher charged ions. In competition with the ionization channel, PAH cations can also fragment upon energetic photoexcitation. This fragmentation follows the available pathways (i.e., dehydrogenation or loss of C_2 or C_2H_2 units), producing PAH derivative species along a top-down chemical scenario (Zhen et al. 2014a; Bouwman et al. 2016; Petrignani et al. 2016). Photoionization and photofragmentation compete, and their relative importance depends on both the geometry of PAH molecules and the excitation wavelengths used (Zhen et al. 2015, 2016).

[4] The ionization parameter is given by the ratio of the ionization rate over the recombination rate and scales with $G_0 T^{1/2}/n_e$, with G_0 the strength of the radiation field in terms of the average interstellar radiation field, T the temperature, and n_e the electron density (Tielens 2005).

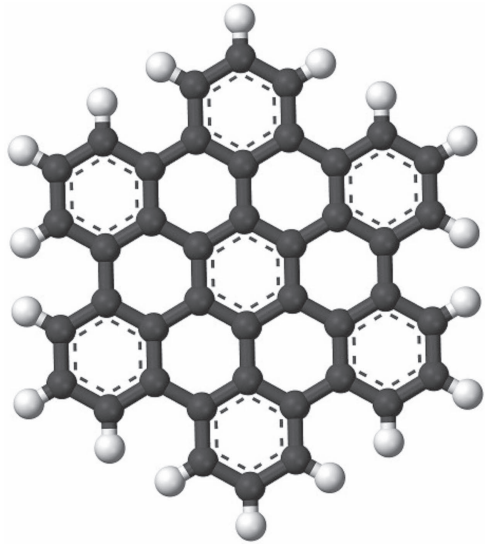

Figure 1. Molecular geometry of hexa-peri-hexabenzocoronene (HBC, $C_{42}H_{18}$).

In order to elucidate possible AIB carriers, neutral and ionized PAH molecules with different size and molecular geometries have been studied, in both the laboratory and by theory. Experimentally, IR spectra of PAH neutrals, cations, and other derivatives have been measured in rare gas matrices (e.g., Szczepanski & Vala 1993a, 1993b; Hudgins & Allamandola 1995a, 1995b; Mattioda et al. 2003; Bernstein et al. 2007; Tsuge et al. 2016). In the gas phase, IR emission spectra have been studied for neutral PAHs and PAH cations (Cook et al. 1998; Kim et al. 2001; Kim & Saykally 2002). Absorption gas-phase spectra of PAH cations have been studied using IR multiphoton dissociation (IRMPD; Oomens et al. 2001, 2006) or messenger atom photodissociation spectroscopy (Piest et al. 1999; Duncan 2003; Douberly et al. 2008; Ricks et al. 2009). A recent application shows that this method is even suited to study fullerene cations (Campbell et al. 2015; Kuhn et al. 2016). While some PAH spectral bands approximately coincide with prominent AIBs, the agreement is not always compelling. A more convincing overlap with astrophysical emission spectra is obtained with composite spectra that consist of (selected) distributions of spectra of different PAH and PAH^+ species that have been recorded using matrix isolation spectroscopy or computed using DFT calculations (Peeters et al. 2002; Cami 2011).

For technical reasons, IR laboratory studies of PAHs have largely been focused on smaller species, containing up to 24 C-atoms. IR spectra of large interstellar relevant PAHs (~50 C-atoms) are generally lacking, and this is also definitely the case for their cations or dications. In this article, we present the first IR spectra of the cation and dication of hexa-peri-hexabenzocoronene: $C_{42}H_{18}^+$ and $C_{42}H_{18}^{2+}$. The resulting IR spectra are compared with quantum chemical computations and astronomical data. HBC (Figure 1) has been selected as it is an all-benzenoid PAH with a size in the astrophysically relevant range (Tielens 2008; Croiset et al. 2016) that possibly serves as a prototypical example for large(r) PAHs. Moreover, the molecular geometry of this PAH is special, as it has only CH groups with a "triply adjacent" or "trio" CH-structure, as shown in Figure 1. This allows us to unambiguously identify the wavelength of the out-of-plane CH bending mode(s) for such a geometry.

2. Experimental Methods

The IR spectra of the fully benzenoid hexa-peri-hexabenzocoronene cation ($C_{42}H_{18}^+$ with $m/z = 522.14$) and its dication ($C_{42}H_{18}^{2+}$) with $m/z = 261.07$) have been recorded using our instrument for photodissociation of PAHs (i-PoP) connected to the Free Electron Laser for InfraRed eXperiments (FELIX) at Radboud University (Oepts et al. 1995). The apparatus comprises a quadrupole ion-trap (QIT) time-of-flight (TOF) mass spectrometer and has been described in detail in Zhen et al. (2014b). Below only a brief description of the relevant details is given.

Neutral HBC precursor molecules are transferred into the gas phase by heating HBC powder (Kentax, purity higher than 99.5%) in an oven (~580 K) until it slowly evaporates. The sublimated HBC molecules are ionized using electron impact ionization (83 eV electron impact energy). The resulting HBC^+ and HBC^{2+} cations are transported into the ion trap via an ion gate and are trapped by applying a 1 MHz radiofrequency electric field of 3150 and 2130 $V_{p.p.}$, respectively, onto the ring electrode. Helium is introduced continuously into the trap to thermalize the ion cloud through collisions.

Spectral information is obtained over the 530–1800 cm^{-1} range by IRMPD using FELIX. This free electron laser delivers 5 μs long macropulses of light at a repetition rate of 10 Hz with a macropulse energy of up to 100 mJ. The bandwidth of the laser is Fourier limited and is typically 0.6% (FWHM) of the central wavelength. When the laser wavelength is in resonance with an allowed vibrational transition in the ion, the absorption of multiple photons takes place, causing the molecule to dissociate. The resulting fragments are then pulse-extracted from the ion trap and analyzed in a TOF mass spectrometer. All channels corresponding to photofragmentation of the parent are summed and normalized to the total signal, i.e., parent plus photofragment ions in the trap, yielding the relative photofragmentation intensity. The IR spectrum of the ion is constructed by plotting the fragment ion yield as a function of wavelength. The recorded spectra are normalized to the pulse energy to correct for any power dependencies.

Mass spectra data for HBC^+ and HBC^{2+} are recorded typically with steps of 5 cm^{-1}. Optimal irradiation times amount to 0.8 s (typically ~8 pulses). In order to obtain a good signal-to-noise ratio, mass spectra are averaged 25 times. In addition, blank spectra are recorded in order to subtract fragmentation peaks that are already present in the background signal.

3. Results and Discussion

Figure 2 shows the mass spectra of the photoproducts that result upon excitation of the 762 cm^{-1} band of HBC^+ (panel A) and the 766 cm^{-1} band of HBC^{2+} (panel B). The mass spectra before irradiation (labeled as background) reveal a small amount of residual fragmentation due to the electron impact ionization and also include ^{13}C isotopes that contribute to the main mass peak signal. The different graphs in Figure 2(A) show the fragmentation patterns of trapped HBC^+ for a set of wavelengths between 750 and 780 cm^{-1}. Several dehydrogenated fragment ions can be seen that are the consequence of multiple and cumulative photon absorptions. The photodissociation pattern follows mainly sequential 2H (or H_2) loss channels, similarly to what was observed for HBC^+ in Zhen et al. (2014b) upon irradiation with optical photons

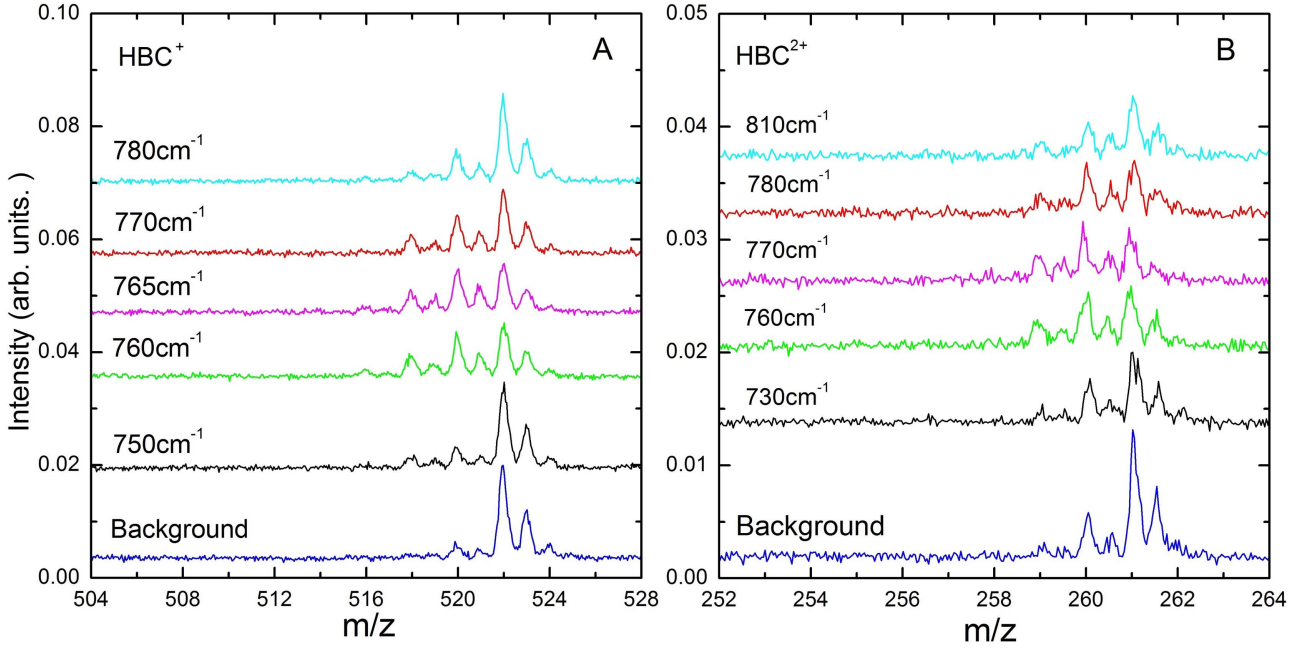

Figure 2. Mass spectrum of the photoproducts resulting from irradiation of HBC^+ and HBC^{2+}: (A) The photodehydrogenation behavior of HBC^+, irradiated at different wavelength in the 762 cm^{-1} band range, and (B) the photodehydrogenation behavior of HBC^{2+}, irradiated at different wavelengths in the 766 cm^{-1} band range. Additional peaks in the background trace are isotopes and fragmentations induced by the electron gun.

(532 nm). Figure 2(B) shows the same data for HBC^{2+}, now after irradiation with wavelengths between 730 and 810 cm^{-1}. Similar to the photofragmentation behavior of HBC^+, a wide range of partially dehydrogenated fragment ions is found, and in the case of HBC^{2+}, the photodissociation pattern also mainly follows sequential 2H (or H_2) losses.

Figure 3 shows the resulting IR spectra for HBC^+ (panel A) and HBC^{2+} (panel B) from 530 to 1800 cm^{-1} (5.6–18.9 μm). The spectra are recorded by integrating the fragmentation signals that vary with wavelength, as illustrated in Figure 2. This figure shows a number of clearly resolved vibrational bands, with reasonable signal-to-noise ratios, even in the case of HBC^{2+}. Many of the bands are rather broad, which is commonly observed for IRMPD spectra and is attributed to anharmonic effects induced by the multiphoton process. It is also possible that broad unresolved bands hide underneath the separate bands visible here. This broadening may be less prominent in experiments using rare gas ion tagging. Such experiments, however, may come with the drawback that transitions substantially shift upon complexation, depending on where the atom tags to the PAH. So far, the existing tagging experiments are available mainly for smaller PAH cations, and they are most likely also hard to apply to dications. An extension to larger species is needed to directly compare with the results presented here.

We also include in Figure 3 the theoretical predictions of the vibrational band positions of HBC^+ and HBC^{2+} (Boersma et al. 2014) that have been scaled by a uniform factor of 0.958 to correct for anhamonicities.[5] In the case of HBC^{2+}, we considered both the singlet and triplet states, but the singlet state was chosen for comparison as it is lowest in energy (Boersma et al. 2014). Table 1 summarizes all vibrational and computed wavelengths with their assignments. The vibrational peak positions are determined directly from the maximum intensity without fitting the overall spectrum. The latter prohibits an overfitting of our data as we do not know how many broad bands may contribute to the overall profile.

Figure 3(A) and Table 1 compare our experimental IRMPD HBC^+ spectrum with the theoretical predictions (Boersma et al. 2014). The most prominent bands include the carbon ring distortions at 1280 (7.81), 1379 (7.25), and 1530 (6.54) cm^{-1} (μm), and the CH in- or out-of-bending modes at 762 (13.12), 1060 (9.43), and 1192 (8.39) cm^{-1} (μm). The intense band at 762 cm^{-1} with a FWHM of ~20 cm^{-1} in the IRMPD spectrum corresponds to the 779 cm^{-1} feature in the DFT spectrum, which arises from out-of-plane CH bending modes. The bands measured at 1060 and 1192 cm^{-1} are close to transitions predicted at 1077 and 1223 cm^{-1}, which arise from in-plane CH bending modes. The experimental bands at 1280 and 1379 cm^{-1} are close to the theoretically predicted bands at 1289 and 1374 cm^{-1}. It is possible that the 1280 cm^{-1} band also includes bands at 1303 and 1308 cm^{-1}. All these bands have a FWHM of ~60 cm^{-1}. The band at 1530 cm^{-1} is broad —with a FWHM of ~120 cm^{-1}—and is probably composed of a number of bands predicted at 1482, 1549, 1559, and 1579 cm^{-1} (Table 1).

Figure 3(B) and Table 1 provide similar information for HBC^{2+}. The error bars here are larger due to a lower ion signal, as fewer dications are trapped in the QIT. The most prominent bands again include the carbon ring distortions at 1290 (7.75), 1370 (7.30), and 1530 (6.54) cm^{-1} (μm) and the CH in- or out-of-bending modes at 660 (15.15), 766 (13.05), 1054 (9.49), and 1176 (8.50) cm^{-1} (μm). The bands at 660 and 766 cm^{-1} with FWHMs of ~20 cm^{-1} in the IRMPD spectrum correspond to the bands at 675 and 785 cm^{-1} in the DFT spectrum, which arise from out-of-plane CH bending modes. The band

[5] This global scaling factor corrects approximately for the shifts in peak position due to anharmonicity at 0 K (Langhoff 1996). This is an approximation as individual bands show different anharmonic corrections in the calculations (Mackie et al. 2016). We also stress that this does not account for the anharmonic shifts in peak position of highly excited species inherent to the IRMPD technique (Oomens et al. 2003).

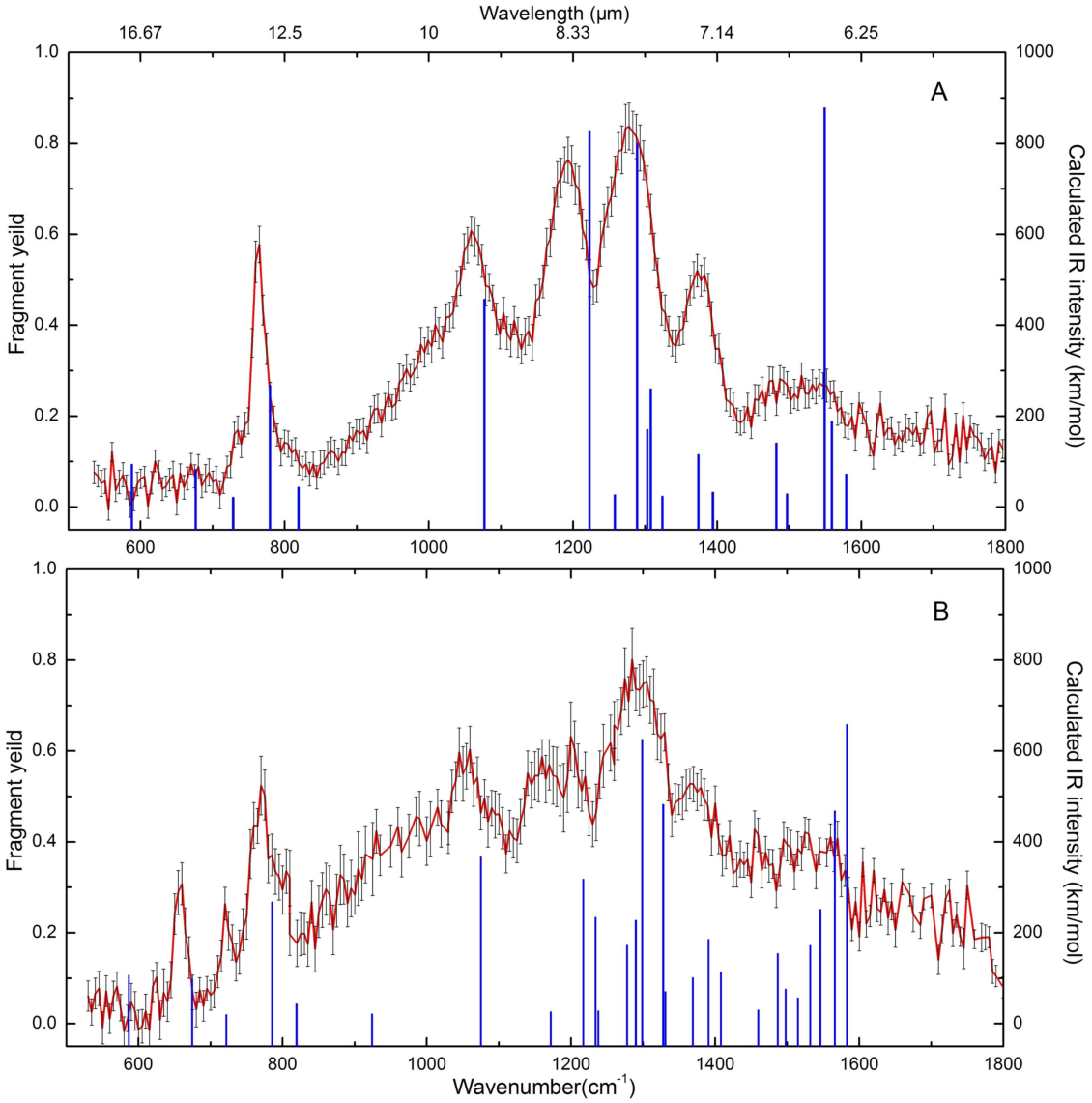

Figure 3. Measured IRMPD spectrum of gas-phase HBC^+ and HBC^{2+}. Computed vibrational normal modes scaled to correct for anharmonicities (taken from Boersma et al. 2014) are represented by vertical bars.

measured at 1054 cm^{-1} is close to the transition predicted at 1075 cm^{-1} and the band at 1176 cm^{-1} in the IRMPD spectrum links to bands at 1217 and 1234 cm^{-1}, which arise from in-plane CH bending modes. The band measured at 1290 cm^{-1} corresponds to the bands computed at 1299 and 1328 cm^{-1} and possibly also contains contributions from nearby bands at 1278, 1290, and 1328 cm^{-1}. The band at 1370 cm^{-1} in the IRMPD spectrum is found in the DFT calculations at 1391 cm^{-1} and possibly also contains contributions from the computed 1369 and 1408 cm^{-1} bands (Table 1). All these bands have a FWHM of ∼60 cm^{-1}. The band at 1530 cm^{-1} is a broad band with a FWHM of ∼120 cm^{-1} and very likely contains contributions from other bands calculated at 1487, 1532, 1546 1566, and 1583 cm^{-1} (Table 1).

As a general point, we emphasize that although a scaling factor of 0.958 is already applied, all experimentally measured band positions of HBC^+ and HBC^{2+} are redshifted with respect to the calculated positions. We attribute this shift to the large anharmonicity associated with the high internal excitation required for the dissociation of large PAHs, which is inherent to the IRMPD technique (Oomens et al. 2003). We note that these shifts are different for different vibrational modes. For example, from Figure 3(A) and Table 1 it becomes clear that the 1192 cm^{-1} band is about ∼30 cm^{-1} situated to lower energy than predicted, whereas for the 1280 cm^{-1} band the shift is only ∼10 cm^{-1}. Taking this into account, the agreement between the experimental values presented here and the available theoretical data is reasonable.

While overall the comparison between experiments and theory is very encouraging, there are also some issues. The HBC^+ and HBC^{2+} bands at 1060 and 1054 cm^{-1}, respectively, exhibit seemingly broad wings toward lower frequencies in the 850−1000 cm^{-1} range. Theory does not predict vibrational normal modes in this region, and these broad bands may be examples of the extreme effects of anharmonicity on IRMPD spectra. As another discrepancy with theory, we note that theory predicts bands at 588 and 587 cm^{-1} for HBC^+ and HBC^{2+}, respectively, which are not apparent in the experiments. Perhaps anharmonicity is also a factor here, shifting these bands outside of the spectral range scanned with FELIX.

Table 1
Infrared Transitions Measured and Calculated for HBC^+ and HBC^{2+}

HBC^+			HBC^{2+}			
Experimental Band cm^{-1}, μm	Computed Band cm^{-1}	Computed Band km mol^{-1}	Experimental Band cm^{-1}, μm	Computed Band cm^{-1}	Computed Band km mol^{-1}	Assignment
	262	33	…	264	23	…
	588	94	…	587	106	…
	676	82[a]	660 (m, A), 15.15	675	98	out-of-plane CH bending
732, (w[b], A[c]), 13.66	728	21	720 (w, B), 13.89	722	20	out-of-plane CH bending
762 (s, B), 13.12	779	267	766 (s, A), 13.05	785	268	out-of-plane CH bending
	819	43	804 (w, B), 12.44	819	43	out-of-plane CH bending
	…	…	…	924	21	…
1060 (s, B), 9.43	1077	457	1054 (s, B), 9.49	1075	367	in-plane CH bending
	…	…	…	1172	26	…
1192 (s, B), 8.39	1223	828	1176 (s, B), 8.50	1217	318	in-plane CH bending
	…	…	…	1234	234	…
	…	…	…	1238	28	…
	1258	26	…			
	…	…	…	1278	172	…
	…	…	…	1290	227	…
1280 (s, B), 7.81	1289	800	1290 (s, B), 7.75	1299	625	carbon ring distortions
	1303	170	…			
	1308	259	…			
	1324	23	…	1328	482	…
	…	…	…	1331	70	…
	…	…	…	1369	101	…
1379 (s, B), 7.25	1374	115	1370 (s, B), 7.30	1391	185	carbon ring distortions
	1394	32	…			
	…	…	…	1408	114	…
	…	…	…	1460	30	…
	1482	140	…	1487	154	…
	1497	29	…	1498	76	…
	…	…	…	1515	57	…
	…	…	…	1532	172	…
	…	…	…	1546	251	…
1530 (m, C), 6.54	1549	878	1530 (m, C), 6.54	1566	468	carbon ring distortions
	1559	188	…	1583	658	…
	1579	72	…			

Notes.
[a] Vibrational frequencies were scaled by a factor of 0.958 to allow comparison with the experimental data, consistent with the recommended scaling for this level of theory (Scott & Radom 1996), and intensities (km mol^{-1}) are given in parentheses. We only list bands with intensities higher than 20 km mol^{-1}.
[b] Relative intensities of experimental bands are indicated as w, m, and s for weak, medium, and strong, respectively.
[c] The uncertainty in the experimental band positions is estimated—following the NIST definition—to be A (1 ∼ 3 cm^{-1}), B (3 ∼ 6 cm^{-1}), and C (15 ∼ 30 cm^{-1}).

In addition, the nonlinear intensity response of IRMPD in combination with a lower output power at the low (and high side) of the accessible wavelength domain may also be responsible for this observation.

One further difference occurs at high frequencies where DFT calculations predict a strong band for HBC^+ at 1549 cm^{-1} and for HBC^{2+} at 1583 cm^{-1} with a number of relatively weaker bands nearby (Table 1). In contrast, instead of one strong band, the experiments reveal weak but broad features between 1430 and 1630 cm^{-1}. This difference may again reflect extreme anharmonicity for these modes. Likewise, we do detect the theoretically predicted band at 660 cm^{-1} of HBC^{2+}, but a similarly predicted band of HBC^+ is missing in our spectrum. On the one hand, this may indicate an issue with the theoretical spectrum of HBC^+. In addition, this might result from a much larger anharmonicity in HBC^+ (than in HBC^{2+}), which would shift this band rapidly out of resonance in our experiment before fragmentation can occur. Further experiments and quantum chemical calculations are required to improve our understanding of these observations.

4. Astrophysical Relevance and Conclusions

This paper presents the first IR spectrum of a PAH cation with an astrophysically relevant size—$C_{42}H_{18}$—in the gas phase. In addition, this is the first time that the spectrum of a PAH dication has been measured experimentally in the gas phase. The experimental IR spectra for both HBC^+ and HBC^{2+} (top two traces) are shown together with typical AIB emission spectra (bottom two traces) in Figure 4. The astronomical emission spectra are from NGC 6946 and NGC 4569 (Smith et al. 2007). This interstellar spectrum shows the well-known prominent broad AIBs at 6.2, 7.7, 8.6, 11.2, and 12.7 μm. As shown in the figure, the experimental spectra of HBC^+ and HBC^{2+} exhibit similarities to several of the key bands in the AIB spectrum. The strong bands at 7.7 and 8.6 μm in the laboratory spectrum closely match the positions of the AIB

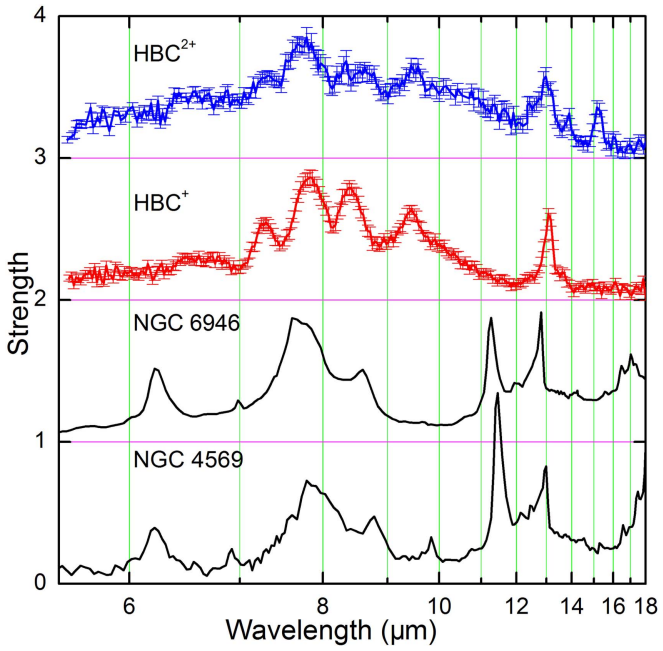

Figure 4. IR spectra of HBC^+ and HBC^{2+} (top) compared to two representative AIB emission spectra (bottom) taken toward NGC 6946 and NGC 4569 and adopted from Smith et al. (2007).

bands at these wavelengths, and the 13.1 μm band is very close to the 12.7 μm band due to trio CH-structure bending modes in HBC. The 11.2 μm band that is detected in the astronomical spectrum is absent in the HBC data, as this band is due to solo CH-structure excitation (Hony et al. 2001) and this group is not present in HBC. This comparison therefore also illustrates that the astronomical spectra may be a combination of emission features originating from many separate species, and HBC^+ and HBC^{2+} probably contribute, but not at a level that allows an unambiguous identification.

Theoretical and experimental studies have highlighted the large spectral differences between neutral and ionized PAHs (Langhoff 1996; Allamandola et al. 1999). As charging involves the delocalized π electron system (rather than the localized σ electrons), bond strength and mode distribution do not differ much between these charge states. The change in charge distribution does influence the change in dipole moment during the vibration, however, and this is the underlying cause for the striking spectral differences. Our experiments show that —in contrast to the neutral-cation behavior—there is no clear spectral signature that can lead to the unambiguous identification of dications in space. This is unfortunate, as a tool for determining the charge state of PAHs in space would substantially contribute to our knowledge on how PAHs behave upon irradiation. The main difference occurs in the 600–700 cm^{-1} region, where a band at 660 cm^{-1} in HBC^{2+} is present in both our experimental study and in the DFT calculations, but the corresponding theoretical band in HBC^+ is not observed in the IRMPD study. As argued above, this may reflect a difference in anharmonicity between HBC^{2+} and HBC^+—rather than a spectral signature of dications—that adversely affects the measured spectra. Further studies are required to address this issue.

The strong transitions in the 530–1800 cm^{-1} (5.6–18.9 μm) IR fingerprint region have been compared to published DFT data, and we conclude that despite drawbacks that complicate the interpretation of band profiles and band intensities, the applied IRMPD technique provides useful band positions for IR active modes. Specifically, we emphasize that the measured HBC spectra support the assignment (Hony et al. 2001) of the interstellar 12.7 μm band to the CH out-of-plane bending mode associated with trios on (large) PAHs (although a duo assignment for the interstellar band may also be viable; (Bauschlicher et al. 2010)). Finally, we stress that this study demonstrates the potential of IRMPD spectroscopy for much larger species than measured before, and this work paves the way to systematically study even larger PAHs (>60 C-atoms) with our setup in the future.

The authors gratefully acknowledge the FELIX staff for their technical assistance during preparation and the actual beamline shifts. We are grateful to M.J.A. Witlox for technical support. We are grateful to Giacomo Mulas and Tao Chen for many very useful discussions. Studies of interstellar chemistry at Leiden Observatory are supported through advanced-ERC grant 246976 from the European Research Council, through a grant by the Netherlands Organisation for Scientific Research (NWO) as part of the Dutch Astrochemistry Network, and through the Spinoza premie. J.B. acknowledges NWO for a Veni grant (722.013.014). We acknowledge the European Union (EU) and Horizon 2020 funding awarded under the Marie Sklodowska-Curie action to the EUROPAH consortium, grant number 722346.

References

Allamandola, L. J., Hudgins, D. M., & Sandford, S. A. 1999, ApJL, 511, L115
Allamandola, L. J., Tielens, A. G. G. M., & Barker, J. R. 1989, ApJS, 71, 733
Bauschlicher, C. W., Boersma, C., Ricca, A., et al. 2010, ApJS, 189, 341
Bellamy, L. 1958, The Infrared Spectra of Complex Molecules (2nd ed.; New York: Wiley)
Berné, O., Joblin, C., Deville, Y., et al. 2007, A&A, 469, 575
Bernstein, M. P., Sandford, S. A., Mattioda, A. L., & Allamandola, L. J. 2007, ApJ, 664, 1264
Boersma, C., Bauschlicher, C. W., Jr., Ricca, A., et al. 2014, ApJS, 211, 8
Boersma, C., Bregman, J. D., & Allamandola, L. J. 2013, ApJ, 769, 117
Bouwman, J., de Haas, A. J., & Oomens, J. 2016, ChCom, 52, 2636
Cami, J. 2011, in EAS Publications Ser. 46, PAHs and the Universe: A Symposium to Celebrate the 25th Anniversary of the PAH Hypothesis, ed. C. Joblin & A. G. G. M. Tielens (Paris: ESA), 117
Campbell, E. K., Holz, M., Gerlich, D., & Maier, J. P. 2015, Natur, 523, 322
Cook, D. J., Schlemmer, S., Balucani, N., et al. 1998, JPCA, 102, 1465
Croiset, B. A., Candian, A., Berné, O., & Tielens, A. G. G. M. 2016, A&A, 590, A26
Douberly, G. E., Ricks, A. M., Schleyer, P. v. R., & Duncan, M. A. 2008, JChPh, 128, 021102
Duncan, M. A. 2003, IRPC, 22, 407
Genzel, R., Lutz, D., Sturm, E., et al. 1998, ApJ, 498, 579
Hony, S., Van Kerckhoven, C., Peeters, E., et al. 2001, A&A, 370, 1030
Hudgins, D. M., & Allamandola, L. J. 1995a, JPhCh, 99, 3033
Hudgins, D. M., & Allamandola, L. J. 1995b, JPhCh, 99, 8978
Kim, H.-S., & Saykally, R. J. 2002, ApJS, 143, 455
Kim, H.-S., Wagner, D. R., & Saykally, R. J. 2001, PhRvL, 86, 5691
Knorke, H., Langer, J., Oomens, J., & Dopfer, O. 2009, ApJL, 706, L66
Kuhn, M., Renzler, M., Postler, J., et al. 2016, NatCo, 7, 13550
Langhoff, S. R. 1996, JPhCh, 100, 2819
Mackie, C. J., Candian, A., Huang, X., et al. 2016, JChPh, 145, 084313
Mattioda, A. L., Hudgins, D. M., Bauschlicher, C. W., Rosi, M., & Allamandola, L. J. 2003, JPCA, 107, 1486
Oepts, D., van der Meer, A. F. G., & van Amersfoort, P. W. 1995, InPhT, 36, 297

Oomens, J., Sartakov, B. G., Meijer, G., & von Helden, G. 2006, IJMSp, 254, 1
Oomens, J., Sartakov, B. G., Tielens, A. G. G. M., Meijer, G., & von Helden, G. 2001, ApJL, 560, L99
Oomens, J., Tielens, A. G. G. M., Sartakov, B. G., von Helden, G., & Meijer, G. 2003, ApJ, 591, 968
Peeters, E., Hony, S., Van Kerckhoven, C., et al. 2002, A&A, 390, 1089
Petrignani, A., Vala, M., Eyler, J. R., et al. 2016, ApJ, 826, 33
Piest, H., von Helden, G., & Meijer, G. 1999, ApJL, 520, L75
Puget, J. L., & Leger, A. 1989, ARA&A, 27, 161
Rapacioli, M., Joblin, C., & Boissel, P. 2005, A&A, 429, 193
Ricks, A. M., Douberly, G. E., & Duncan, M. A. 2009, ApJ, 702, 301
Scott, A. P., & Radom, L. 1996, JPhCh, 100, 16502
Sellgren, K. 1984, ApJ, 277, 623
Smith, J. D. T., Draine, B. T., Dale, D. A., et al. 2007, ApJ, 656, 770
Szczepanski, J., & Vala, M. 1993a, ApJ, 414, 646
Szczepanski, J., & Vala, M. 1993b, Natur, 363, 699
Tielens, A. G. G. M. 2005, The Physics and Chemistry of the Interstellar Medium (1st ed.; Cambridge: Cambridge Univ. Press)
Tielens, A. G. G. M. 2008, ARA&A, 46, 289
Tielens, A. G. G. M. 2013, RvMP, 85, 1021
Tsuge, M., Bahou, M., Wu, Y.-J., Allamandola, L. J., & Lee, Y.-P. 2016, ApJ, 825, 96
Zhen, J., Castellanos, P., Paardekooper, D. M., et al. 2015, ApJL, 804, L7
Zhen, J., Castellanos, P., Paardekooper, D. M., Linnartz, H., & Tielens, A. G. G. M. 2014a, ApJL, 797, L30
Zhen, J., Castillo, S. R., Joblin, C., et al. 2016, ApJ, 822, 113
Zhen, J., Paardekooper, D. M., Candian, A., Linnartz, H., & Tielens, A. G. G. M. 2014b, CPL, 592, 211